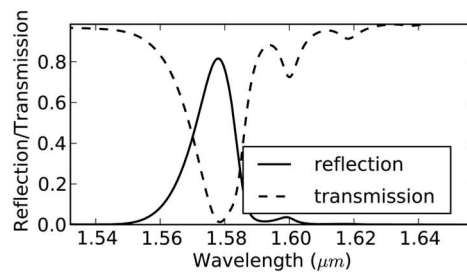


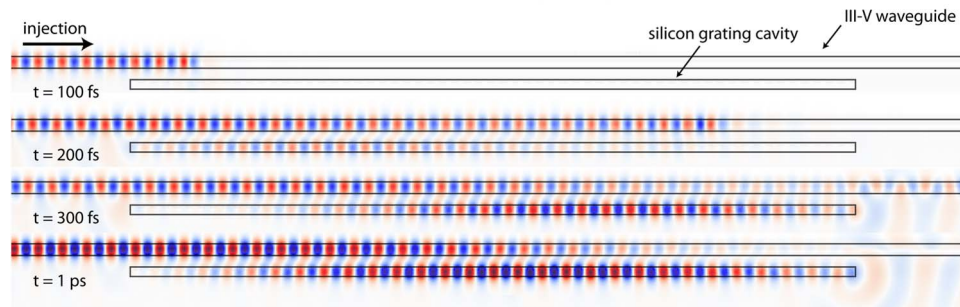
# Design of a Hybrid III–V-on-Silicon Microlaser With Resonant Cavity Mirrors

Volume 5, Number 2, April 2013

Y. De Koninck  
G. Roelkens  
R. Baets



(a)



(b)

DOI: 10.1109/JPHOT.2013.2259586  
1943-0655/\$31.00 ©2013 IEEE

# Design of a Hybrid III–V-on-Silicon Microlaser With Resonant Cavity Mirrors

Y. De Koninck, G. Roelkens, and R. Baets

Photonics Research Group, Department of Information Technology, Ghent University—IMEC,  
Center for Nano- and Biophotonics (NB-photonics), B-9000 Ghent, Belgium

DOI: 10.1109/JPHOT.2013.2259586  
1943-0655/\$31.00 ©2013 IEEE

Manuscript received April 8, 2013; accepted April 15, 2013. Date of current version April 29, 2013. This work was supported in part by the Agency for Innovation by Science and Technology (IWT) through the strategic basic research (SBO) project GlucoSens and in part by the European Research Council through the InSpectra project. The work of Y. De Koninck was supported by Research Foundation Flanders (FWO). Corresponding author: Y. De Koninck (e-mail: yannick.dekoninck@intec.ugent.be).

**Abstract:** A novel approach is presented to realize compact III–V-on-silicon microlasers. The concept relies on resonant mirrors in which the close interaction between a III–V waveguide and an underlying silicon cavity provides high narrow-band reflection back into the III–V waveguide. Combining two such mirrors with a III–V waveguide in between leads to a resonant mirror laser. The properties of the resonant mirror are studied for a variety of device parameters. Using this information, the properties of the resulting laser, such as threshold power and side-mode suppression ratio, are investigated. These calculations correspond well to proof-of-concept experimental results.

**Index Terms:** Silicon photonics, heterogeneous III–V integration, lasers, bonding, microlasers, microcavity.

## 1. Introduction

Over the last decade, silicon has grown to be one of the most important material systems available for integrated photonic components and circuits. Combining the mature fabrication technology inherited from CMOS electronics with the high refractive index contrast between the silicon waveguide core and its surrounding cladding allows for unprecedented miniaturization and integration of passive optical components as well as high-speed modulators and detectors. Unfortunately, silicon has an indirect bandgap, making it unsuitable as a laser gain material. Over the years, a number of approaches have been proposed to enable laser sources on silicon-based nanophotonic platforms. Examples are epitaxial growth of a direct-bandgap III–V material on top of the silicon substrate [1], exploiting nonlinear photon interaction in the silicon itself [2], or using strained and doped germanium on top of the silicon layer as a laser gain medium [3]. However, the most performant approach to date is the so-called hybrid III–V-on-silicon integration. A III–V semiconductor die with an epitaxial structure grown on top is bonded upside down onto a patterned silicon-on-insulator (SOI) die using either molecular or adhesive bonding [4]. After the III–V substrate is removed, the remaining III–V film (thickness from below 100 nm to a few micrometers) is patterned using a series of lithography and etching steps. Finally, metal contacts are added to obtain the desired laser structure.

A number of hybrid laser types have been presented over the last years. DFB and DBR lasers were demonstrated using both molecular [5] and adhesive [6] bonding. In both cases, the optical mode is mainly confined to the passive silicon layer, but its evanescent tail reaches into the III–V overlay where it experiences optical gain. This approach results in relatively large devices ( $> 400 \mu\text{m}$ ) and,

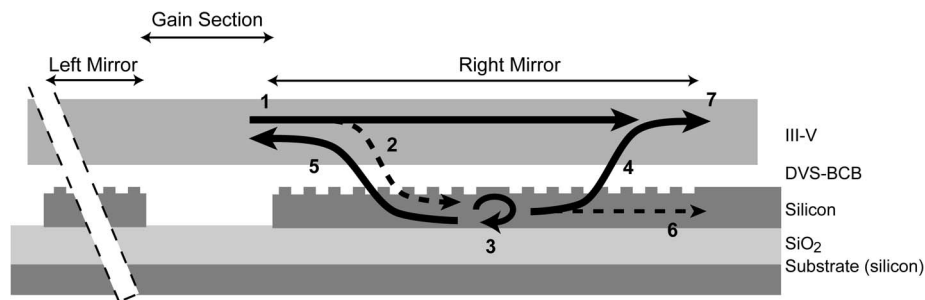


Fig. 1. **Schematic side view of a heterogeneously integrated Si/III–V laser with resonant mirrors.** The different arrows illustrate the operation of the grating cavity as a mirror. The dimensions on this scheme are not to scale, especially the length of the gain section is greatly reduced for the sake of clarity.

consequently, a high threshold current ( $> 20$  mA). However, reducing the laser threshold current to shrink the overall power consumption is of paramount importance in many applications. One way to reduce the threshold current is to scale down the physical size of the laser. Examples of such so-called microlasers are III–V microdisk lasers [7], linear III–V photonic crystal cavity lasers [8], and photonic crystal mirror VCSELs [9]. The threshold pump power for these microlasers is on the order of 1 mW or less. Electrically injected microdisk lasers have been demonstrated, but the disk cavity supporting whispering gallery modes lacks an inherent wavelength selection mechanism to prevent mode hopping and multimode lasing. The linear III–V photonic crystal laser and the photonic crystal mirror VCSEL laser are inherent single-mode laser cavities, but electrical injection has not yet been demonstrated. In this paper, we propose a novel design for heterogeneously integrated III–V-on-silicon microlasers that promises to enable small-footprint single-mode lasers with precise wavelength control and a low laser threshold. In the first part of this paper, we will introduce the general concept of the proposed laser, which revolves around the concept of resonant cavity mirrors. We will also provide an in-depth discussion of a number of mirror designs and the influence of the different parameters on the reflectivity spectrum. In the second part, we will discuss how this mirror fits in the overall laser design and estimate the expected laser characteristics.

### 1.1. Resonant Cavity Mirror Lasers

The general layout of the proposed laser concept is depicted in Fig. 1. Like any other laser, this design consists of two mirror sections with an active gain section in between. The gain section consists of a III–V waveguide with no silicon waveguide underneath (*Gain Section* in Fig. 1). In other words, the optical mode traveling through the gain section is fully confined to the III–V waveguide. This way, the overlap between the optical mode and the active layer in the gain section is optimized. In each mirror section, a silicon grating cavity lies underneath the III–V waveguide. This can be a finite grating that supports a number of band-edge resonances or a grating with a quarter-wave shift that supports a localized defect resonance. When the light propagating in the III–V waveguide reaches the section with the silicon cavity underneath (1 in Fig. 1), a small fraction couples (2) to the silicon resonator. If the wavelength of the light is close to the silicon cavity resonance wavelength, power will start to build up in this cavity (3). If the energy contained in the silicon cavity is high enough, a significant amount of light will couple back into the III–V waveguide. The light coupling back codirectionally to the III–V waveguide (4) will interfere destructively with the light that did not couple to the silicon cavity, yielding, in the ideal case, no transmission through the III–V waveguide (7). The light that couples back into the III–V waveguide counterdirectionally to the incident light (5) will provide the feedback necessary for laser operation. Since this is a resonant phenomenon, the reflection bandwidth of this mirror will be narrow, which is useful for single-mode operation. Although the size of the mirror structure largely depends on actual cavity implementation, we will propose designs where the mirror is shorter than  $30 \mu\text{m}$ . This approach to implementing compact wavelength-selective optical feedback also provides an elegant mechanism to couple the generated laser light to an

external silicon waveguide. *Because of the resonance, there is already a large energy buildup inside the silicon cavity. By extending the silicon waveguide beyond the grating, a small amount of light can tunnel out of the cavity into the silicon waveguide (6). This waveguide can lead the generated laser light anywhere on the photonic integrated circuit. Alternatively, a waveguide can be brought into close proximity next to the cavity to directionally couple some of the light in the silicon cavity to the waveguide. The amount of coupling can be determined by the spacing between the waveguide and the cavity.*

This interplay between a III–V waveguide and a silicon cavity underneath that results in narrow-band reflection back into the III–V waveguide is called a *resonant mirror*. The combination of two such mirrors with a III–V gain section in between is a resonant mirror laser. The laser wavelength is determined by the overlap between the active material's gain spectrum, the narrow reflectivity spectrum of the mirrors, and the spectral position of the longitudinal modes in the III–V waveguide. For this type of laser, nearly all important laser parameters, such as lasing wavelength, threshold power, and side-mode suppression ratio (SMSR), are, to a large extent, determined by the reflectivity spectrum of the resonant mirror. This work will, therefore, first investigate the reflectivity spectrum of different resonant mirror designs using full-vectorial 3-D FDTD simulations. For each design, the influence of the predominant parameters in the system will be explained. Second, the calculated spectrum is used to estimate laser properties such as threshold power and SMSR.

### 1.1.1. Technology Platform and Simulation Tools

In this paper, the silicon waveguide structure is assumed to be fabricated on a standard 220-nm SOI platform: On top of the silicon substrate lies a 2- $\mu\text{m}$ -thick silicon oxide layer ( $n_{\text{SiO}_2} = 1.45$ ) that is covered with another 220-nm-thick silicon layer ( $n_{\text{Si}} = 3.477$ ). The silicon grating cavities are strip waveguides (220-nm etch) with 70-nm-deep etched corrugations. The choice for this particular waveguide structure is motivated by the fact that it can be fabricated in a widespread and mature technological process based on CMOS fabrication processes. Also, many passive optical components with excellent properties have been demonstrated in this technology. To enable close integration of optical functions, the silicon layer of the laser source and the passive silicon components should be fabricated in the same technology. However, the conclusions that will be drawn from the simulations performed in this particular material system can be extended to any other high-index-contrast technology.

The silicon die is covered by a thin layer of divinylsiloxane benzocyclobutene (DVS-BCB –  $n_{\text{BCB}} = 1.55$ ) as this is the material used for adhesive bonding. *To avoid bubbling of the BCB, the patterned silicon die can be planarized with SiO<sub>2</sub> prior to bonding. This way, high-quality ultrathin bonding layers can be achieved [10]. Alternatively, molecular bonding can be used.* The III–V layer is 240 nm thick and consists of an 80-nm bulk InGaAsP active layer ( $n_{\text{InGaAsP}} = 3.57$ ) sandwiched between nonintentionally doped InP layers ( $n_{\text{InP}} = 3.1649$ ). The waveguide in the III–V layer is 1.6  $\mu\text{m}$  wide. To simplify the analysis, the III–V waveguide has no electrical contacts. To pump the active region, the structure is illuminated from the top with a pump laser beam. It is possible to pump the active region electrically, for example, by using lateral injection as proposed in [11], but this is outside the scope of this paper.

Throughout this paper, we make extensive use of the open-source 3-D FDTD package MEEP [12]. Reflection and transmission spectra are calculated by launching a short pulse into the III–V waveguide and measuring the reflected and transmitted power flux in the same waveguide.  $Q$ -factors are extracted using harmonic inversion [13] of the electric field time trace inside the cavity after the initial excitation has faded out. Dispersion diagrams are calculated using the open-source package MPB [14]. TE polarized light is used throughout this paper.

## 2. Band-Edge Resonators

*The dispersion diagram in Fig. 2(a) relates the wave vector of the fundamental guided TE mode to its vacuum wavelength in a 1.6- $\mu\text{m}$ -wide silicon waveguide grating (period = 285 nm, duty cycle 50%). The figure shows that this particular grating does not support propagating modes between*

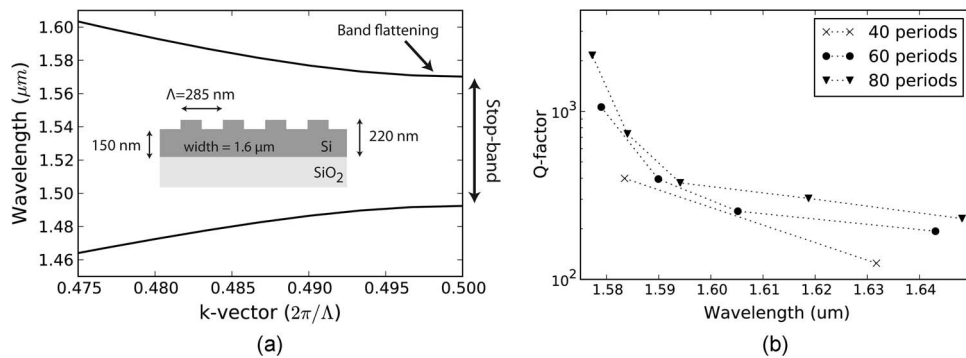


Fig. 2. (a) Dispersion diagram for a silicon waveguide grating with dimensions as indicated in the figure showing the grating's stopband. (b) Resonance wavelengths (indicated by the scatter points) and corresponding  $Q$ -factors for the band-edge resonances in such a waveguide grating. The different curves are for different cavity lengths. The dotted line serves as a guide to the eye to connect the different resonances in the same structure.

$\lambda = 1492$  nm and  $\lambda = 1570$  nm, the *grating's stopband*. A direct consequence of this *stopband* is the flattening of the dispersion curve near the edges of the band where  $d\omega/dk$  (hence also  $d\lambda/dk$ ) reaches zero at  $k = \pi/\Lambda$ . Since group velocity  $v_g$  is proportional to  $d\omega/dk$ , the guided modes near the edge of the band will have a decreased group velocity and are called 'slow-light' modes.

In a grating of finite length, the mode experiences reflection at the facets, leading to Fabry–Perot resonances. However, due to their low group velocity, it takes the modes near the band-edge a longer time to travel through the cavity, increasing the  $Q$ -factor significantly as compared with Fabry–Perot cavities of similar length and facet reflectivity. For a more in-depth theoretical treatment of band-edge resonances, see [15].

### 2.1. Intrinsic Cavity Properties

Fig. 2(b) shows the frequencies and corresponding  $Q$ -factors for the band-edge resonances of a 1.6- $\mu\text{m}$ -wide silicon grating cavity. *Only the resonances at the low-energy side of the band (1570 nm instead of 1490 nm) are considered because these are the Bloch modes that are mainly concentrated in the higher parts of the grating. Consequently, these resonances are more confined to the silicon layer, leading to lower out-of-plane leakage and a higher  $Q$ -factor.* These  $Q$ -factors are for the intrinsic grating cavities, so there is a thin layer of BCB on top of the gratings but no III–V waveguide. The grating period is 285 nm (50% duty cycle). The different curves in Fig. 2(b) are for 40, 60, and 80 periods. For such short cavity lengths and in the absence of material absorption, the predominant loss mechanism in this type of cavity that limits the  $Q$ -factor is leakage from the grating's end facets. That explains why the  $Q$ -factor is maximum near the bandgap and increases with an increasing number of periods: In both cases, it takes the photons a longer time to travel between the facets. As could be expected from a Fabry–Perot-like cavity, increasing the number of periods (so increasing the cavity length) will increase the spectral resonance density. On the other hand, spectral spacing between different resonances is not constant as in a classic Fabry–Perot resonator, but increases as the group velocity increases when going away from the band-edge.

### 2.2. Band-Edge Resonators Used as Resonant Mirrors

Fig. 3(a) shows typical reflection and transmission spectra of a resonant mirror with a band-edge grating resonator. This spectrum was calculated by launching the fundamental eigenmode into the III–V waveguide (1 in Fig. 1) and collecting the reflected eigenmode in the same location. The transmission spectrum was also calculated in the III–V waveguide at position 7 in Fig. 1.

In this particular example, the silicon cavity consists of a 60-period grating with a 285-nm pitch. The distance between the top of the silicon waveguide and the bottom of the III–V waveguide (the *bonding layer thickness*) is 300 nm. The silicon waveguide grating is 1.6  $\mu\text{m}$  wide, and the

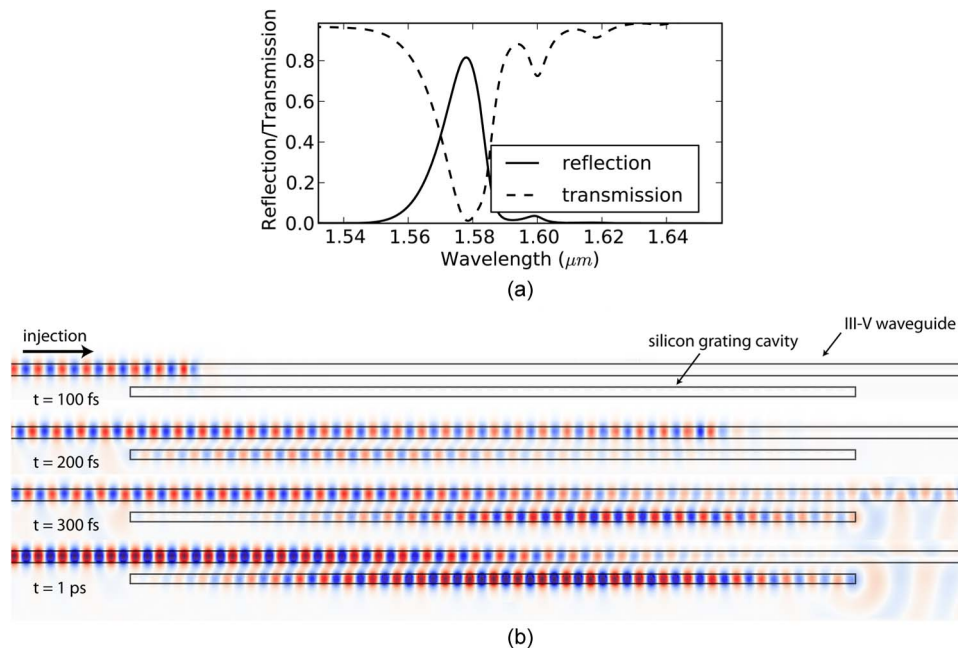


Fig. 3. (a) Reflection and transmission spectra of a resonant mirror using a silicon band-edge cavity with 60 periods and a grating pitch of 285 nm. (b) Field profiles through a cross section at different points in time for CW injection (at resonance wavelength) of the same structure.

III–V waveguide is 1.5  $\mu\text{m}$  wide. At the resonance wavelength (1577.95 nm), the total reflection back into the III–V waveguide is 81.65%, while only 2% is transmitted through the III–V waveguide. The reflection bandwidth (FWHM) is 14 nm. Consequently, the  $Q$ -factor for the loaded system (silicon cavity + III–V waveguide) is 112.7. This is considerably lower than the silicon cavity's intrinsic  $Q$ -factor ( $\approx 1000$ ), which means that the loss in the silicon cavity is now dominated by coupling to the III–V waveguide.

To gain more insight into the operation of the mirror, Fig. 3(b) shows the electric field in a cross section similar to that in Fig. 1 at four different points in time. A CW signal ( $\lambda = 1578$  nm, the mirror's resonance wavelength) is injected into the III–V waveguide ( $t = 100$  fs). Only a small fraction of the light in the III–V waveguide couples to the silicon cavity ( $t = 200$  fs), and most of the light propagates through the III–V waveguide ( $t = 300$  fs). Once the energy in the silicon cavity is sufficiently high ( $t = 1$  ps), light is reflected back into the III–V waveguide. Consequently, light is no longer transmitted through the III–V waveguide. The electric field amplitude in the III–V waveguide is higher at  $t = 1$  ps because the forward (incoming) wave and the backward (reflected) wave both propagate through the same waveguide, giving rise to a standing wave. The same figure also clearly shows that most of the light that is not reflected leaks away from the right-hand side of the silicon cavity. This light can be collected by adding a silicon waveguide at the end of the cavity to serve as an output port of the laser, as described in Section 1.1.

*The reflection spectrum of the resonant mirror strongly depends on the geometry of the silicon cavity. Inevitable fabrication errors in the silicon layer, such as a deviation in grating fill-factor or etch-depth, will change the effective index of the silicon cavity mode. This, in turn, will shift the resonance wavelength of the cavity and, consequently, the laser wavelength. If necessary, it is possible to bring a thermal tuning mechanism in close proximity to the silicon cavity to control its refractive index and, therefore, its resonance wavelength.* Yet, the most important properties of a resonant mirror based on band-edge resonances, maximum reflectivity and reflection bandwidth, are mainly determined by the  $Q$ -factor of the silicon cavity and the degree of coupling between the silicon cavity and the III–V waveguide. These two properties are predominantly controlled by the length of the silicon

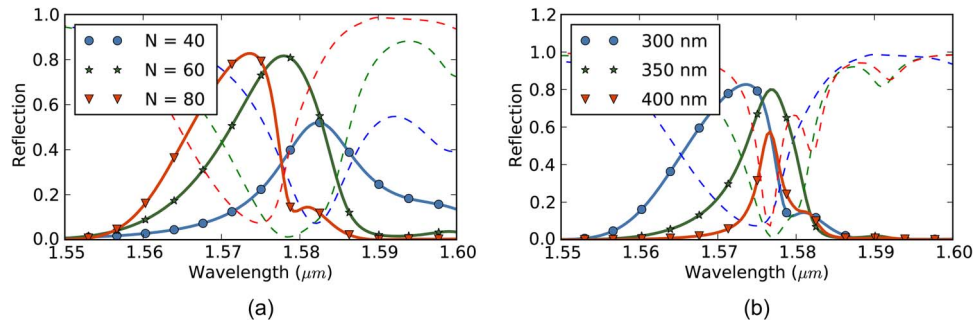


Fig. 4. Influence of the number of periods (a) and BCB thickness (b) on the reflection spectrum of a band-edge resonant mirror. Except for the variable parameter, the structure is identical to the one presented in Fig. 3. Solid lines are reflection spectra, dashed lines are transmission spectra.

grating and the bonding layer thickness. The next two paragraphs will elaborate on the influence of these two design parameters.

### 2.2.1. Influence of Grating Length

Fig. 4(a) shows the reflection (solid) and transmission (dashed) spectra for three different mirrors. The three mirrors are identical to the structure in the previous paragraph [see Fig. 3(a)] except for the number of periods in the silicon grating. When increasing the length of the silicon grating, three things happen. First, the resonance wavelengths of the resonances in the intrinsic cavity shift toward shorter wavelengths, as can be seen in Fig. 2(b). Second, the  $Q$ -factor of these resonances increases [also in Fig. 2(b)]. Finally, because the band-edge mode is not localized but spread out along the length of the grating, increasing the number of grating periods will increase the interaction length between the III–V waveguide and the silicon cavity.

These three effects explain the behavior of the different spectra in Fig. 4(a). The wavelengths of the reflection maxima in Fig. 4(a) correspond to the resonance wavelengths in Fig. 3(b). When increasing the grating length from 40 periods to 60 periods, the maximum reflectivity increases from around 50% to 81.6%. This is the result of both the increase in the  $Q$ -factor and the longer interaction length, increasing the coupling. For 60 periods, the power transmitted through the III–V waveguide is almost zero. This indicates that the cavity is critically coupled to the III–V waveguide. If the number of periods is increased to 80, the maximum reflectivity only slightly increases from 81.6% to 82.6%. The amount of power that is transmitted through the III–V waveguide increases to around 10%. This indicates that the III–V waveguide is no longer critically coupled to the silicon cavity. Even though the reflection is slightly higher, this situation is not desirable because only 10% of the incoming light can be coupled to the silicon output waveguide and 10% is lost when transmitted through the III–V waveguide. In the critically coupled case (60 periods), almost no light is lost through the III–V waveguide, and the fraction of power that is directed to the silicon waveguide is much higher. The reflection bandwidth does not change significantly when varying the number of grating periods.

### 2.2.2. Influence of Bonding Layer Thickness

Fig. 4(b) shows reflection and transmission spectra for resonant mirrors with 80-period-long silicon gratings and a bonding layer thickness of 300 nm, 350 nm, and 400 nm. All other parameters are identical to the structure presented in Fig. 3. Varying the bonding layer thickness mainly affects the coupling between the III–V waveguide and the silicon cavity. For this particular configuration, the system is critically coupled if the bonding layer thickness is 350 nm (zero transmission through the III–V waveguide).

Similar to the discussion in Section 2.2.1, the maximum reflectivity for the overcoupled system is slightly higher than the critically coupled case, but again, this configuration is not desirable because 10% of the incident light is lost through the III–V waveguide. Increasing the bonding layer thickness

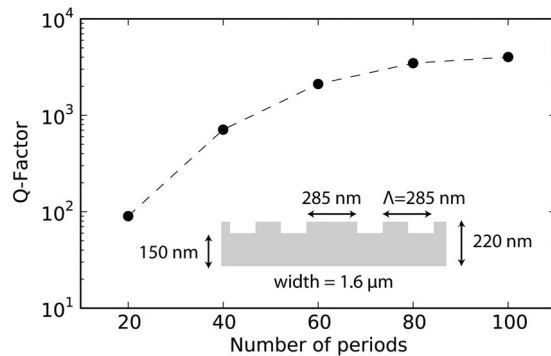


Fig. 5.  $Q$ -factor of the intrinsic defect resonators for different cavity lengths. The dimensions of the cavity are as indicated in the figure. The defect is always located in the center of the grating.

will reduce the coupling between the III–V waveguide and the silicon cavity and, in turn, reducing the maximum reflectivity. The FWHM bandwidth of the reflection peak also clearly reduces for increasing bonding layer thickness. The wavelength for peak reflectivity is weakly dependent on the bonding layer thickness. For a thinner bonding layer thickness, the evanescent tail of the silicon cavity mode feels the presence of the III–V waveguide on top, slightly changing the resonance wavelength of the combined system.

### 3. Defect Resonators

#### 3.1. Introduction

By adding a defect to the periodic silicon grating, the structure now supports a localized mode within the stopband. Light in the defect is trapped between two barriers, which can lead to a resonator with higher  $Q$ -factors than band-edge resonators of equal length. The inset in Fig. 5 shows how the defect is introduced by adding a quarter-wave shift to the grating waveguide discussed in Section 2.

#### 3.2. Intrinsic Cavity Properties

Fig. 5 plots the intrinsic cavity  $Q$ -factor as a function of the total number of periods of the structure. The defect is always located in the center of the grating (for example: for a total number of 60 periods, the defect is between two gratings of 30 periods each). The resonance wavelength is independent of the number of periods and is 1534 nm in this particular case (285-nm pitch).

The  $Q$ -factor saturates to a value around 4000 for cavities with 100 periods or more. In this case, the primary loss mechanism is scattering at the defect. It is possible to increase the  $Q$ -factor even more by carefully designing the size of the defect to reduce the out-of-plane scattering by canceling out different radiation fields with opposing signs [16]. This requires very low tolerances on the exact defect size, which is not realistic given the current state-of-the-art processing. In this paper, we will not try to optimize the  $Q$ -factor further.

#### 3.3. Defect Resonators Used as Resonant Mirrors

Fig. 6(a) shows typical reflection and transmission spectra for a resonant mirror with a defect cavity. The grating has 60 periods, and the dimensions are as shown in the inset in Fig. 5. The III–V waveguide is identical to the one in Section 2, and the bonding layer thickness is 300 nm. This structure is similar to the band-edge resonant mirror in Fig. 3 except for the quarter-wave shift in the silicon grating. The reflection and transmission spectra also seem similar: In both cases, the maximum reflectivity is around 80%, and no light is transmitted through the III–V waveguide. However, there are subtle differences between both configurations. The maximum reflectivity is at a shorter wavelength, corresponding to the center instead of the edge of the bandgap in Fig. 2(a). Even

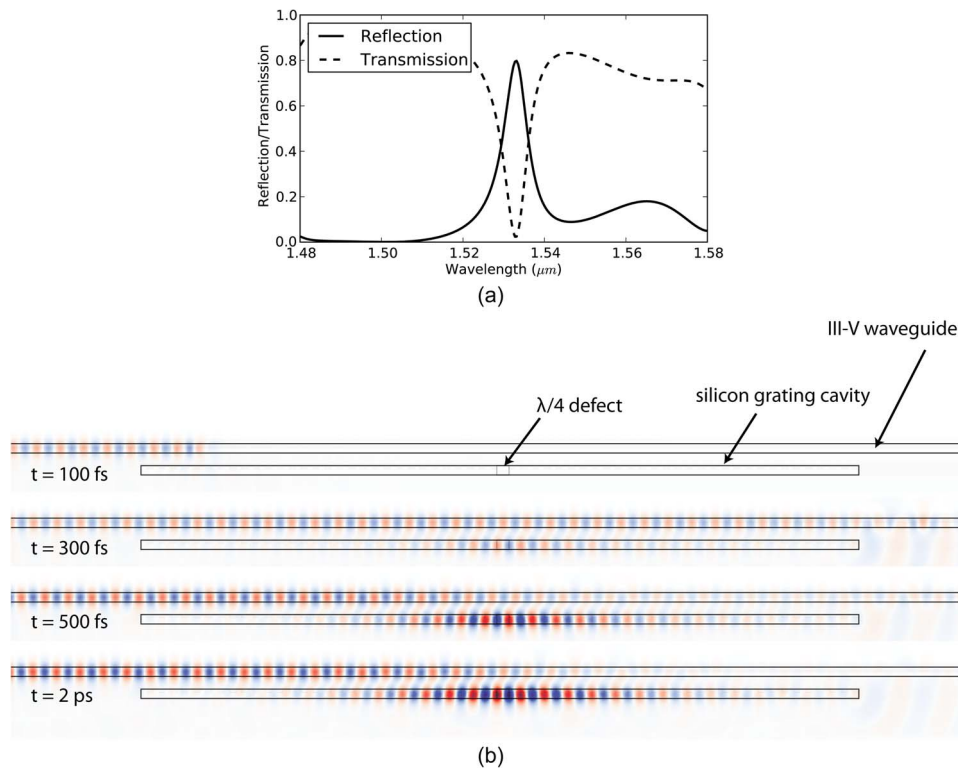


Fig. 6. (a) Typical spectrum for a resonant mirror with defect cavity. This particular example is for a 60-period grating with a defect in the center. The grating pitch is 285 nm, and the bonding layer thickness is 300 nm. (b) Field profiles at different points in time for CW injection at the cavity resonance wavelength.

though the bonding layer thickness and the grating length are the same, the reflection bandwidth of the defect resonant mirror is half (7 nm) the reflection bandwidth of the corresponding band-edge resonant mirror (14 nm). The reason for this is that the field profile of the defect resonance is not spread out along the length of the grating but is localized around the quarter-wave defect. Consequently, the interaction length between the traveling mode in the III–V waveguide and the resonance mode in the silicon grating is shorter, reducing the coupling between both.

Fig. 6(b) shows the electric field in a cross section similar to that in Fig. 1 at different points in time. The cavity dynamics are slower than the dynamics of the band-edge cavity, which was already indicated by the narrower line width. The figure also shows that the resonance mode is localized around the defect, resulting in a shorter interaction length with the propagating mode in the III–V waveguide.

Similar to the treatment on band-edge resonators, the next two paragraphs will deal with the influence of the grating length and bonding layer thickness on the reflection spectrum of the defect-based resonant mirror.

### 3.3.1. Influence of Grating Length

In Fig. 7(a), the reflection and transmission spectra for different grating lengths are depicted. Again,  $N$  is the total number of grating periods. The device parameters are similar to the resonant mirror in Fig. 6 except for the number of periods in the silicon grating. As stated before, the field profile of the silicon cavity mode is localized around the quarter-wave defect. Consequently, its shape and spatial extent, hence the interaction length with the III–V waveguide mode, is only weakly dependent on the number of periods in the grating. Therefore, the coupling between the III–V waveguide and the silicon cavity can be considered independent of the number of periods in the grating. This is also indicated by the fact that the structure is always close to critical coupling

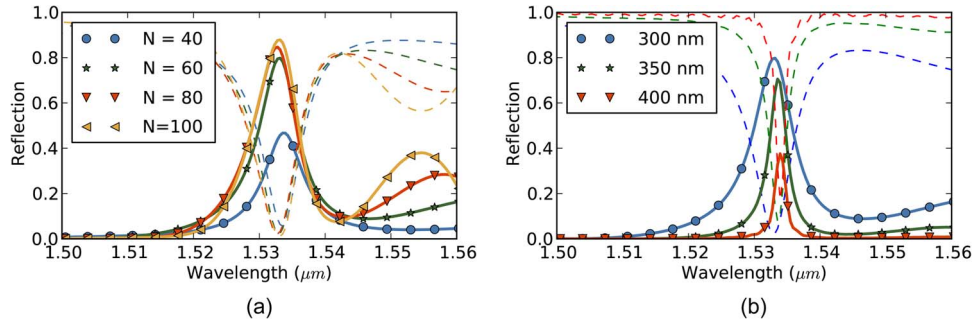


Fig. 7. Influence of the number of periods (a) and BCB thickness (b) on the reflection spectrum of a defect cavity resonant mirror. Except for the varied parameter, the structure is identical to the one presented in Fig. 6. Solid lines are reflection spectra, dashed lines are transmission spectra.

(no transmission through the III–V waveguide), regardless of the number of periods in the grating. If the silicon cavity is critically coupled to the III–V waveguide, the maximum reflectivity is mainly determined by the  $Q$ -factor of the cavity and varies from 50% for  $N = 40$  periods to 88% for  $N = 100$  periods.

### 3.3.2. Influence of Bonding Layer Thickness

Fig. 7(b) shows the reflection and transmission spectra for the defect resonant mirror in Fig. 6 for three different values of the bonding layer thickness. This graph is similar to Fig. 4(b). By increasing the bonding layer thickness, the coupling between the III–V waveguide and the silicon cavity is decreased. Consequently, the maximum reflectivity decreases, and the reflection bandwidth becomes narrower.

## 4. Laser Properties

To design a laser using the resonant mirrors described in the previous sections, the only parameter left to decide is the distance between the two mirrors. In between the two mirror sections, the light is fully confined to the III–V waveguide, as shown in Fig. 1. The choice of the length of this III–V waveguide between the two mirror sections is important because it will determine the spectral properties (SMSR) and threshold power of the laser.

Fig. 8(a) shows the different longitudinal resonances for a resonant mirror laser with the defect-based grating mirror in Fig. 6 and mirror spacing  $L$  of  $10 \mu\text{m}$ ,  $20 \mu\text{m}$ ,  $50 \mu\text{m}$ , and  $100 \mu\text{m}$ . The dashed line is the reflection spectrum of the mirror [same as in Fig. 6(a)]. The solid lines indicate the different resonances of the laser structure. The resonance wavelengths are calculated by considering the phase shift of the resonant mirror and the phase accumulated when propagating through the III–V waveguide. The length of each laser is slightly adjusted to align the peak of the resonant mirror's reflection spectrum to one of the longitudinal resonances. The amplitude of each bar in Fig. 8(a) is the modal gain  $g_{\text{th}}$  (in  $\text{cm}^{-1}$ ) required in the III–V waveguide to reach lasing threshold. The modal threshold gain is calculated by assuming no internal losses in the III–V waveguide, so:  $g_{\text{th}} = \ln(R^2)/2L_{\text{tot}}$ .  $L_{\text{tot}}$  is the total length the light travels in the III–V waveguide. To a good approximation, this is the distance between the two defects in the silicon cavities, so  $L_{\text{tot}} \approx L + 17 \mu\text{m}$ , because each silicon grating is about  $17 \mu\text{m}$  long, and the defect is in the center of the grating. Fig. 8(b) shows the electric field distribution through a cross section of a device with  $L = 20 \mu\text{m}$ . The figure also shows how  $L$  and  $L_{\text{tot}}$  are defined.

If modal threshold gain  $g_{\text{th}}$  is known, the most important laser properties can be calculated by considering the differential equation describing the time evolution of carrier density  $N(t)$  in the laser's active region

$$\frac{dN(t)}{dt} = \frac{P(t)}{h\nu_p V_a} - AN(t) - BN^2(t) - CN^3(t) - v_g G(N)S(t). \quad (1)$$

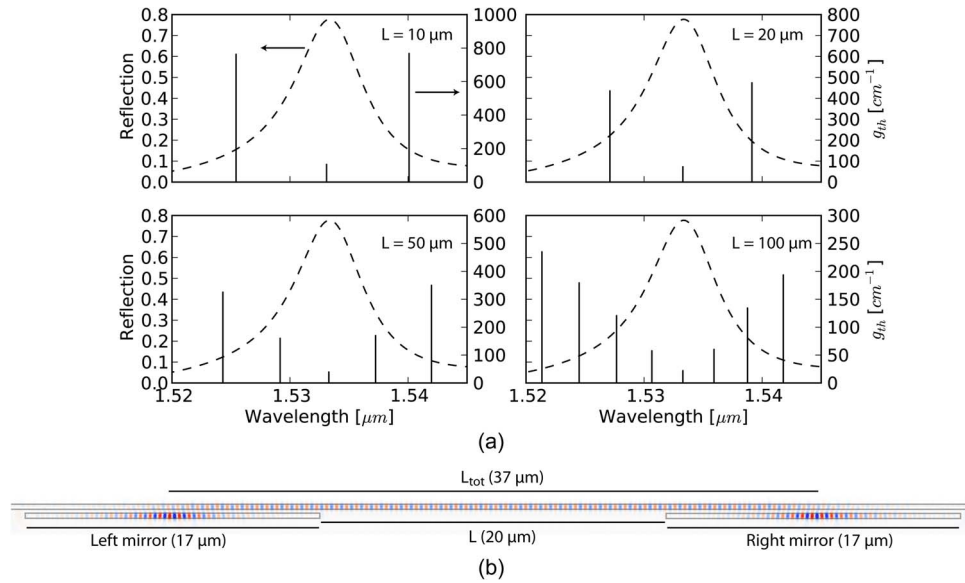


Fig. 8. (a) Resonances of the laser structure for different values of the spacing  $L$  between the resonant mirror structures. The dashed curve is the reflection spectrum of the resonant mirror that is used (identical to that in Fig. 6). The height of each bar representing a laser resonance is the modal gain required to reach threshold for that particular resonance. (b) Field distribution of the resonant laser mode with the lowest threshold gain for a 20- $\mu\text{m}$  spacing between the resonant mirrors.

In this equation,  $P(t)$  is the pump power absorbed in the active region,  $h$  is Planck's constant,  $\nu_p$  is the frequency of the pump beam,  $V_a$  is the volume of the active region,  $A$  is the Shockley–Read–Hall recombination coefficient,  $B$  is the spontaneous recombination coefficient,  $C$  is the Auger recombination coefficient,  $v_g$  is the group velocity of the fundamental mode in the III–V waveguide,  $G(N)$  is the carrier-dependent material gain, and  $S(t)$  is the cavity's photon density. Assuming a bulk InGaAsP active layer, the material gain in the active layer depends linearly on the carrier density

$$G(N) = G_0(N - N_0). \quad (2)$$

In this equation,  $G_0$  is the differential gain, and  $N_0$  is the transparency carrier density. Modal gain  $g$  is related to material gain  $G$  by the confinement factor  $\Gamma$  of the fundamental eigenmode of the III–V waveguide:  $g = \Gamma G$ . With this relationship, the carrier density  $N_{\text{th}}$  required to reach threshold can be calculated using equation (2). Next, the threshold pump power  $P_{\text{th}}$  is calculated by setting  $dN/dt$  and  $S$  to zero, assuming  $N = N_{\text{th}}$  and solving equation (1) for  $P$ .

Photon density  $S$  in the III–V waveguide is

$$S = \frac{P - P_{\text{th}}}{h\nu_p v_g \Gamma G_{\text{th}} V_a}. \quad (3)$$

Consequently, laser output power  $P_{\text{out}}$  is

$$P_{\text{out}} = \eta h\nu_l \frac{V_a}{\Gamma} \frac{v_g}{2L_{\text{tot}}} S = \eta \frac{\nu_l}{\nu_p} \frac{P - P_{\text{th}}}{2L_{\text{tot}} g_{\text{th}}}. \quad (4)$$

In this equation,  $\eta$  is the fraction of the mirror's incident power that is coupled into the silicon output waveguide, and  $\nu_l$  is the laser frequency. The SMSR can be calculated using [17]

$$\text{SMSR} = \frac{\Delta g_{\text{th}}}{g_{\text{th}}} \frac{V_a}{\Gamma n_{\text{sp}}} S \quad (5)$$

TABLE 1

Parameters in rate-equation model

Symbol	Parameter	Value	Reference
$A$	SRH-recombination coefficient	$10^8 \text{ s}^{-1}$	[19]
$B$	spontaneous recombination coefficient	$2 \times 10^{-10} \text{ cm}^3 \text{ s}^{-1}$	[19]
$C$	Auger recombination coefficient	$1.63 \times 10^{-28} \text{ cm}^6 \text{ s}^{-1}$	[19]
$v_g$	III-V waveguide group velocity	$10^8 \text{ m s}^{-1}$	simulation
$G_0$	differential gain ( $dG/dN$ )	$3.13 \times 10^{-16} \text{ cm}^2$	[20]
$N_0$	Transparency carrier density	$6.5 \times 10^{17} \text{ cm}^{-3}$	[20]
$\Gamma$	III-V waveguide confinement factor	43.3%	simulation
$\nu_p$	frequency of pump beam	$c/1.0\mu\text{m}$	
$\nu_l$	output frequency of laser	$c/1.55\mu\text{m}$	
$\eta$	transmission to SOI waveguide	15%	simulation
$n_{sp}$	spontaneous emission factor	2	[17]

TABLE 2

Calculated laser properties

$L$ [ $\mu\text{m}$ ]	$P_{th}$ [ $\mu\text{W}$ ]	$P_{out}$ [ $\mu\text{W}$ ] ( $P = 2P_{th}$ )	SMSR [dB]
10	623.	51.8	39.8
20	592.	49.3	40.2
50	658.	55.2	41.4
100	872.	72.8	42.4

where  $n_{sp}$  is the spontaneous emission factor, and  $\Delta g_{th}$  is the difference in modal threshold gain between the main laser mode and the strongest side-mode. Table 2 shows these laser properties for different lengths  $L$  between the mirrors. The parameters used in the calculations are in Table 1. The values for the different laser properties do not vary significantly for the different values of  $L$ . A spacing of 20  $\mu\text{m}$  between the mirrors yields the lowest threshold power. For shorter devices, the threshold gain rises quickly. For longer devices, the threshold gain is low, but the volume of the active region  $V_a$  is large, requiring a large amount of free carriers. The calculated SMSR is very high, around 40 dB in all cases (for  $P = 2P_{th}$ ). These calculations correspond well to our recent experimental results [18] where we demonstrated a resonant mirror laser with mirrors identical to the ones used in this simulation and a mirror spacing of 20  $\mu\text{m}$ . For these devices, we found a threshold power of 0.6 mW (we estimate that 10% of 6-mW incident pump power is absorbed by the InGaAsP layer) and an SMSR of 39 dB.

In calculating the values in Table 2, one of the longitudinal resonances was aligned to the maximum of the mirror's reflection spectrum. In reality, small changes in the effective index of the III–V waveguide will shift the longitudinal resonance wavelength away from the maximum reflectivity and alter the laser properties. Fig. 9 shows how threshold power  $P_{th}$  and SMSR change when the effective index of the III–V waveguide shifts with an amount  $\Delta n$ . Using an optical mode solver, the changes in  $\Delta n$  can be related to changes in width ( $\Delta n/\Delta W = 0.01/200 \text{ nm}$ ), height ( $\Delta n/\Delta H = 0.029/10 \text{ nm}$ ), and temperature ( $\Delta n/\Delta T = 0.024/100\text{K}$  [21]) of the III–V waveguide. The laser wavelength shifts at  $\Delta\lambda/\Delta n = 5 \text{ nm}/0.04$ .

Fig. 9 shows that for the shorter distance between the resonant mirrors, a significant advantage in terms of stability toward changes in the effective index is obtained. Lasers with a spacing between the mirrors of 20  $\mu\text{m}$  or less can easily accommodate a  $\Delta n$  offset of 0.01, which corresponds to a 10% margin on the waveguide width or a 50-K rise in temperature. As can be expected from a thin-film device, all configurations are very sensitive to changes in the thickness of the III–V waveguide, but this can be controlled very accurately using epitaxial growth.

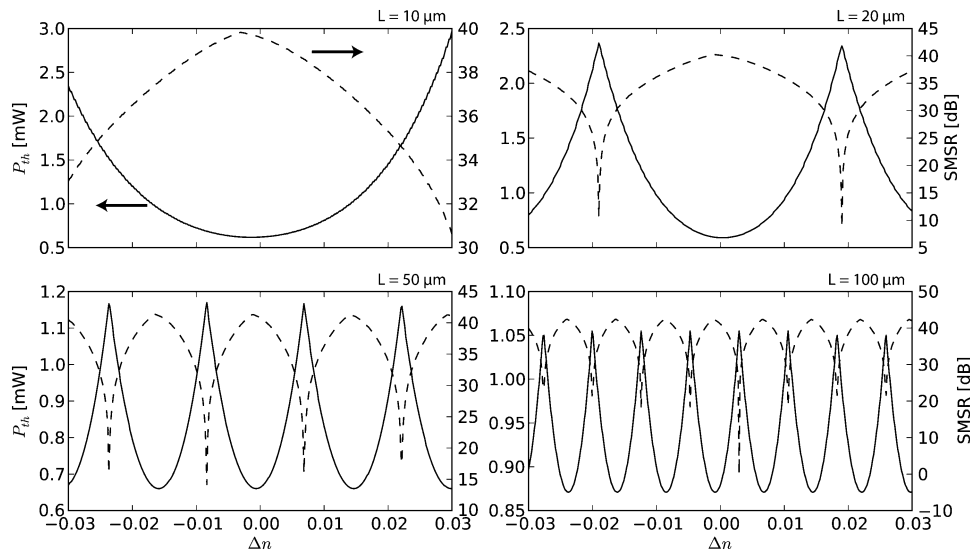


Fig. 9. Threshold power (solid line) and SMSR (dashed line) for changes in  $n_{\text{eff}}$  for different values of the spacing between the resonant mirrors. Changes in  $\Delta n$  can be related to changes in width ( $\Delta n/\Delta W = 0.01/200 \text{ nm}$ ), height ( $\Delta n/\Delta H = 0.029/10 \text{ nm}$ ), and temperature ( $\Delta n/\Delta T = 0.024/100\text{K}$ ) of the III–V waveguide.

According to the previous discussion, the ideal spacing between the two silicon mirrors is between  $10 \mu\text{m}$  and  $20 \mu\text{m}$  for this particular case. For shorter devices, the gain necessary to reach threshold will increase, and the required carrier density will be too high. Longer devices are too sensitive to variations in the effective index of the III–V waveguide, which can result in multimode lasing and unpredictable behavior.

## 5. Conclusion

In this paper, we have presented a novel approach to heterogeneously integrated III–V-on-silicon microlasers, based on the concept of resonant mirrors. We have studied the behavior of such mirrors in two different configurations: using a band-edge grating resonator and a defect grating resonator. In both cases, we investigated how the characteristics of the reflection and transmission spectra changed when the values of the most important parameters were varied. Using the mirror characteristics, the threshold power and SMSR were estimated to be  $600 \mu\text{W}$  and  $40 \text{ dB}$ , respectively. Recent experimental results are in good agreement with these calculations. This work paves the way for the realization of large arrays of single-mode microlasers cointegrated on a silicon chip, with a well controlled lasing wavelength and wavelength spacing. This can be of particular interest for WDM applications or as a source for spectroscopic sensing systems.

## References

- [1] G. Wang, M. Leys, N. Nguyen, R. Loo, G. Brammertz, O. Richard, H. Bender, J. Dekoster, M. Meuris, M. Heyns, and M. Caymax. (2011, Jan.). Growth of high quality InP layers in STI trenches on miscut Si (001) substrates. *J. Cryst. Growth* [Online]. *315*(1), pp. 32–36. Available: <http://linkinghub.elsevier.com/retrieve/pii/S0022024810004902>
- [2] H. Rong, A. Liu, R. Jones, O. Cohen, D. Hak, R. Nicolaescu, A. Fang, and M. Paniccia. (2005, Jan.). An all-silicon Raman laser. *Nature* [Online]. *433*(7023), pp. 292–294. Available: <http://www.ncbi.nlm.nih.gov/pubmed/15635371>
- [3] R. E. Camacho-Aguilera, Y. Cai, N. Patel, J. T. Bessette, M. Romagnoli, L. C. Kimerling, and J. Michel. (2012, May). An electrically pumped germanium laser. *Opt. Exp.* [Online]. *20*(10), pp. 11 316–11 320. Available: <http://www.ncbi.nlm.nih.gov/pubmed/22565752>
- [4] G. Roelkens, L. Liu, D. Liang, R. Jones, A. Fang, B. Koch, and J. Bowers, “III–V/silicon photonics for on-chip and inter-chip optical interconnects,” *Laser Photon. Rev.*, vol. 4, no. 6, pp. 751–779, Nov. 2010.
- [5] A. W. Fang, E. Lively, H. Kuo, D. Liang, and J. E. Bowers, “A distributed feedback silicon evanescent laser,” *Opt. Exp.*, vol. 16, no. 7, pp. 4413–4419, Mar. 2008.

- [6] S. Stankovic, R. Jones, M. N. Sysak, J. M. Heck, G. Roelkens, and D. Van Thourhout, "Hybrid III V / Si distributed-feedback laser," *IEEE Photon. Technol. Lett.*, vol. 24, no. 23, pp. 2155–2158, Dec. 2012.
- [7] J. Van Campenhout, P. R. A. Binetti, P. R. Romeo, P. Regreny, C. Seassal, X. J. M. Leijts, T. D. Vries, Y. S. Oei, R. P. J. V. Veldhoven, R. Nötzel, L. D. Cioccio, J.-M. Fedeli, M. K. Smit, D. V. Thourhout, and R. Baets, "Low-footprint optical interconnect on an SOI chip through heterogeneous integration of InP-based microdisk lasers and microdetectors," *IEEE Photon. Technol. Lett.*, vol. 21, no. 8, pp. 522–524, Apr. 2009.
- [8] Y. Halioua, A. Bazin, P. Monnier, T. J. Karle, G. Roelkens, I. Sagnes, R. Raj, and F. Raineri. (2011, May). Hybrid III–V semiconductor/silicon nanolaser. *Opt. Exp.* [Online]. 19(10), pp. 9221–9231. Available: <http://www.ncbi.nlm.nih.gov/pubmed/21643176>
- [9] C. Sciancalepore, B. B. Bakir, X. Letartre, J. Harduin, N. Olivier, C. Seassal, J.-M. Fedeli, and P. Viktorovitch, "CMOS-compatible ultra-compact 1.55- $\mu\text{m}$  emitting VCSELs using double photonic crystal mirrors," *IEEE Photon. Technol. Lett.*, vol. 24, no. 6, pp. 455–457, Mar. 2012.
- [10] S. Keyvaninia, M. Muneeb, S. Stankovi, P. J. V. Veldhoven, D. V. Thourhout, and G. Roelkens, "Ultra-thin DVS-BCB adhesive bonding of III–V wafers, dies and multiple dies to a patterned silicon-on-insulator substrate," *Opt. Mater. Exp.*, vol. 3, no. 1, pp. 35–46, Jan. 2013.
- [11] P. Viktorovitch, C. Sciancalepore, B. Ben Bakir, X. Letartre, and C. Seassal, "Double photonic crystal vertical-cavity surface-emitting lasers," in *Proc. SPIE Photon. West OPTO*, San Francisco, CA, USA, 2013.
- [12] A. F. Oskooi, D. Roundy, M. Ibanescu, P. Bermel, J. D. Joannopoulos, and S. G. Johnson, "MEEP: A flexible free-software package for electromagnetic simulations by the FDTD method," *Comput. Phys. Commun.*, vol. 181, no. 3, pp. 687–702, Mar. 2010.
- [13] S. G. Johnson. (2006, Nov.). *Harminv*. [Online]. Available: <http://ab-initio.mit.edu/wiki/index.php/Harminv>
- [14] S. G. Johnson and J. D. Joannopoulos. (2001, Jan.). Block-iterative frequency-domain methods for Maxwell's equations in a planewave basis. *Opt. Exp.* [Online]. 8(3), pp. 173–190. Available: <http://www.opticsexpress.org/abstract.cfm?URI=OPEX-8-3-173>
- [15] A. Figotin and I. Vitebskiy, "Gigantic transmission band-edge resonance in periodic stacks of anisotropic layers," *Phys. Rev. E*, vol. 72, no. 3, pp. 036619-1–036619-12, Sep. 2005.
- [16] J. D. Joannopoulos, S. G. Johnson, J. N. Winn, and R. D. Meade, *Photonic Crystals: Molding the Flow of Light*. Princeton, NJ, USA: Princeton Univ. Press, 2007.
- [17] G. Morthier and P. Vankwikelberge, *Handbook of Distributed Feedback Laser Diodes*. Norwood, MA, USA: Artech House, 1997.
- [18] Y. De Koninck, F. Raineri, A. Bazin, R. Raj, G. Roelkens, and R. Baets, "Demonstration of a novel single-mode hybrid silicon microlaser," in *Proc. IEEE IPC*, Sep. 2012, pp. 1–2.
- [19] J. Piprek, *Semiconductor Optoelectronic Devices*. New York, NY, USA: Academic, 2003.
- [20] J. Leuthold, M. Mayer, J. Eckner, G. Guekos, H. Melchior, and C. Zellweger. (2000, Jan.). Material gain of bulk 1.55  $\mu\text{m}$  InGaAsP/InP semiconductor optical amplifiers approximated by a polynomial model. *J. Appl. Phys.* [Online]. 87(1), pp. 618–620. Available: <http://link.aip.org/link/JAPIAU/v87/i1/p618/s1&Agg=doi>
- [21] F. G. Della Corte, G. Cocorullo, M. Iodice, and I. Rendina. (2000, Sep.). Temperature dependence of the thermo-optic coefficient of InP, GaAs, and SiC from room temperature to 600 K at the wavelength of 1.5  $\mu\text{m}$ . *Appl. Phys. Lett.* [Online]. 77(11), pp. 1614–1616. Available: <http://link.aip.org/link/APPLAB/v77/i11/p1614/s1&Agg=doi>